

Investigating the Andromeda Stream: I. Simple Analytic Bulge-Disk-Halo Model for M31

J. J. Geehan^{1*}, M. A. Fardal^{1,2}, A. Babul¹, P. Guhathakurta³

¹*Dept. of Physics & Astronomy, University of Victoria, Elliott Building, 3800 Finnerty Rd., Victoria, BC V8P 1A1, Canada*

²*Dept. of Astronomy, University of Massachusetts, Amherst, MA 01003, USA*

³*UCO/Lick Observatory, Dept. of Astronomy & Astrophysics, Univ. of California, 1156 High St., Santa Cruz, CA 95064, USA*

Accepted 2005 November 10. Received 2005 October 30; in original form 2005 January 13

ABSTRACT

This paper is the first in a series which studies interactions between M31 and its satellites, including the origin of the giant southern stream. We construct accurate yet simple analytic models for the potential of the M31 galaxy to provide an easy basis for calculation of orbits in M31’s halo. We use an NFW dark halo, an exponential disk, a Hernquist bulge, and a central black hole point mass to describe the galaxy potential. We constrain the parameters of these functions by comparing to existing surface brightness, velocity dispersion, and rotation curve measurements of M31. Our description provides a good fit to the observations, and agrees well with more sophisticated modeling of M31. While in many respects the parameter set is well constrained, there is substantial uncertainty in the outer halo potential and a near-degeneracy between the disk and halo components, producing a large, nearly two-dimensional allowed region in parameter space. We limit the allowed region using theoretical expectations for the halo concentration, baryonic content, and stellar M/L ratio, finding a smaller region where the parameters are physically plausible. Our proposed mass model for M31 has $M_{\text{bulge}} = 3.2 \times 10^{10} M_{\odot}$, $M_{\text{disk}} = 7.2 \times 10^{10} M_{\odot}$, and $M_{200} = 7.1 \times 10^{11} M_{\odot}$, with uncorrected (for internal and foreground extinction) mass-to-light ratios of $M/L_R = 3.9$ and 3.3 for the bulge and disk, respectively. We present some illustrative test particle orbits for the progenitor of the stellar stream in our galaxy potential, highlighting the effects of the remaining uncertainty in the disk and halo masses.

Key words: galaxies: M31 – galaxies: kinematics and dynamics

1 INTRODUCTION

The detritus resulting from the disruption and assimilation of a satellite galaxy by its larger host is a veritable treasure trove of clues and information about the galaxy assembly process, the nature of the merging subunits, as well as the dynamical properties of the parent system. Typically in the form of stellar streams, this detritus can remain spatially and kinematically coherent in the halo of the larger galaxy for several billion years (Johnston et al. 1996; Helmi & White 1999). Identifying and quantifying these features in detail, however, is a challenging task as it often entails resolving and measuring properties of individual stars in the stellar halo of the galaxies. At present, such studies are only feasible for the galaxies in the Local Group. The Milky Way stellar halo has been the focus of detailed scrutiny for many years now resulting in the detection of a number of coherent features in the star counts (see

Yanny et al. 2003; Majewski et al. 2004; Martin et al. 2004; Law, Johnston, & Majewski 2005 and references therein). Unfortunately, as noted by Newberg et al. (2002), our vantage point within the Galaxy greatly complicates the interpretation of these features. Consequently, the recent uncovering of rich substructure (Ibata et al. 2001; Ferguson et al. 2002; McConnachie et al. 2003; Morrison et al. 2003; Merrett et al. 2003; Ferguson et al. 2004; Guhathakurta et al. 2004; Zucker et al. 2004; Merrett et al. 2004) in the stellar halo of the Andromeda galaxy (M31) is highly tantalizing.

The most striking of these features is the giant southern stellar stream extending out from the south-eastern part of M31’s disk. First reported by Ibata et al. (2001), the stream stars have since been targeted for careful photometric and spectroscopic analyses resulting in the determination of the distance to the stream at various locations along its length (McConnachie et al. 2003) as well as the measurement of stellar kinematics in a number of locations (Ibata et al. 2004; Guhathakurta et al. 2004). Jointly, these observations indicate that the giant southern stream extends away from us

* E-mail: jgeehan@uvic.ca (JJG), fardal@fcrao1.astro.umass.edu (MF), babul@uvic.ca (AB), raja@ucolick.org (PG)

below the disk of M31, out to a distance of ~ 100 kpc away from the M31 center. There is also a strong velocity gradient along the body of the stream, with the outer regions being at rest with respect to M31 while the inner regions approach us at 300 km s^{-1} with respect to M31.

Intense observational effort notwithstanding, the source of the giant southern stream has yet to be identified. We do not know whether the progenitor survives and if so, where it is, although several faint features in the inner halo of M31, such as the newly detected satellite And VIII (Morrison et al. 2003), have been touted as possibilities. One approach to identifying the progenitor of the stream, or at least its fate, is to reconstruct its orbit using the stream properties as constraints. Both Ibata et al. (2004) and Font et al. (2004) have initiated efforts in this direction. As we shall illustrate, both in this and in Paper II (Fardal et al. 2005), a detailed study of the stream dynamics and of its progenitor orbit, however, requires a realistic, reasonably accurate model for the potential of M31 that is also preferably easy to use and straightforward to alter for experimentation purposes.

The simplest approach to describing the potential of M31 is by modeling the mass distribution in the galaxy. The earliest efforts at doing so date back to Babcock (1938, 1939), followed by a series of investigations by Wyse & Mayall (1942), Kuzmin (1943), Kuzmin (1952), Schwarzschild (1954), and Schmidt (1957) over the course of the next two decades. Subsequent improvement in the quality of photometric and spectroscopic data in the 70s and the 80s led to a reassessment of the mass models by Deharveng & Pellet (1975), Monnet & Simien (1977), Simien, Pellet, & Monnet (1979), and Kent (1989). As heroic as these efforts were, these models were constructed at a time when the shape and the parameters describing dark halos were largely unknown and unconstrained. Most recently, the problem has been revisited by Klypin, Zhao, & Somerville (2002), Widrow, Perrett, & Suyu (2003) and Widrow & Dubinski (2005). However, the mass models put forth by these groups, though sophisticated, are neither simple nor easy to use especially for the purposes of orbit calculations. The Widrow, Perrett, & Suyu (2003) mass models, for example, are specified in terms of a set of distribution functions. While these distribution functions can be used to compute the mass density distribution for M31 as well as the associated gravitational potential, the derivation is implicit and must be solved for iteratively. In other words, a closed-form analytic description of the density and the potential is not available. Similarly, the Klypin et al. model is also not available in closed analytic form.

In this paper, we attempt to remedy this by presenting a reasonably accurate yet simple analytic description of the M31 mass distribution. Our principal aim is to arrive at a description of the gravitational potential that is both suitable for the purposes of computing satellite orbits and sufficiently transparent that it can be easily altered for the sake of experimentation. We achieve this by decomposing the mass distribution in M31 into four components: the central black hole (BH), the bulge, the disk and the extended halo. The components are modelled using well-known functional forms whose associated potentials are easy to compute. The appropriate values of the associated structural parameters are determined by requiring that the model is in agreement with

the observed M31 rotation, surface brightness, and bulge velocity dispersion profiles. In § 2, we describe the analytic functional forms we have chosen for the four components. In § 3, we review the M31 observations used to constrain the structural parameters, and visually compare to our best-fit model. In § 4, we examine the allowed region of parameter space, which shows both strong constraints in some directions and near-degeneracies in others. We discuss additional physical constraints on the solutions besides those used in the fit. Two “constrained best-fit” solutions resulting from this discussion are presented along with those of our formal best-fit solution in Table 2; we direct readers interested only in the final product to this table. In § 5, we briefly illustrate the relevance of our present efforts, by computing sample orbits for the progenitor of the giant southern stream. We discuss the effect of the uncertainty in the potentials on the orbits, and compare our orbits to those obtained in some simple analytic potentials that have been recently used for this purpose. A summary of our key results is presented in § 6. For completeness, we note that our adopted cosmology is a spatially flat Λ CDM universe with $\Omega_m = 0.14h^{-2}$, $\Omega_b = 0.024h^{-2}$, and a Hubble constant of $h = 0.71$ in units of 100 km/s/Mpc .

2 COMPONENTS OF OUR M31 MASS MODEL

In principle, a detailed mass model of M31 ought to comprise of several components: the central black hole, the nucleus, the bulge, the bar, the spheroid, the thick and thin stellar disks and the thin gaseous disk. In the interest of simplicity, we restrict ourselves to only four components: the central BH, the bulge, the disk and the extended halo. Moreover, our use of simple analytic functions to describe these components necessitates making some simplifying assumptions. We discuss these as well as our choice of functional forms below.

2.1 The Central Black Hole

The very central region of M31 is comprised of a central BH and a distinct small-scale stellar nuclear component that is photometrically and dynamically separate from the bulge and the large-scale galactic disk (see Kormendy & Richstone 1995 and references therein). The most recent estimate of the BH mass is $M_\bullet = (5.6 \pm 0.7) \times 10^7 M_\odot$ (Salow & Statler 2004), while the mass of the stellar component is estimated to be $\lesssim 2 \times 10^7 M_\odot$, within $\sim 10 \text{ pc}$ (Bacon et al. 2001; Peng 2002; Salow & Statler 2004).

In terms of the total M31 potential, the two nuclear components are only relevant on scales $r < 20 \text{ pc}$ and for all practical purposes, can be ignored in the context of the calculations of interest to us. However, to facilitate wider use of our M31 model, we include the dynamically more important of the two, the BH component, in the form of a point mass located at the center of our galaxy, and fix its mass to the value quoted above. The inclusion of this component is necessary, for example, in order to correctly model the velocity components in the nucleus of M31 (cf. Figure 3).

2.2 The Galactic Bulge

We model the bulge of M31 as a spherically symmetric mass distribution represented by a Hernquist profile (Hernquist 1990):

$$\rho_b(r) = \left(\frac{M_b}{2\pi r_b^3} \right) \frac{1}{(r/r_b)(1+r/r_b)^3}, \quad (1)$$

where M_b is the total mass of the bulge and r_b is its scale radius. The mass profile and the potential corresponding to this density distribution are

$$M_b(r) = \frac{M_b r^2}{(r_b + r)^2}, \quad (2)$$

$$\Phi_b(r) = -\frac{GM_b}{r_b + r}. \quad (3)$$

We considered using the more general density profile of Dehnen (1993) where $\rho_b(r) \propto (r/r_b)^{-\gamma}(1+r/r_b)^{\gamma-3}$ but found that the results for $0.1 \leq \gamma \leq 2$ were all equally good. For simplicity, we have opted to use the $\gamma = 1$ Hernquist profile. We also note that the both the bulge mass and the bulge mass-to-light ratio are quite insensitive to variations in γ within the range noted. This gives us confidence that the bulge parameters that we quote in Table 2, and more generally our bulge-disk decomposition, are robust regardless of the precise nature of the inner density structure in the bulge.

On the other hand, using a spherical model for the bulge is clearly a simplification. Detailed modeling based on surface photometry suggests that at the very least, the bulge ought to be modelled as an oblate spheroid with axis ratio of ~ 0.8 (Kent 1983, 1989; Peng 2002; Widrow, Perrett, & Suyu 2003) and that in actuality, it is almost certainly triaxial (Lindblad 1956; Stark 1977; Kent 1989; Stark & Binney 1994; Berman 2001; Berman & Loinard 2002). In opting to avoid the complications of using a non-spherical mass distribution, we are primarily guided by the purpose of this paper, which is to construct orbits to model the giant southern stream. This stream has a pericenter estimated to be at ~ 2 to 4 kpc, and an apocenter of ~ 100 kpc (Ibata et al. 2004; Font et al. 2004), so it spends little to no time in a region where the asphericity of the bulge could have any dynamical effect. After all, the equipotential surfaces tend to spheres at large radii even if the density distribution does not. However, if our models are used to treat dynamics at smaller radii, the reader should keep this simplification in mind.

2.3 The Galactic Disk

In order to model the M31 galactic disk, we begin by assuming, as suggested by the observations of Waltherbos & Kennicutt (1987), that the disk mass distribution can be described by an exponential surface density profile:

$$\Sigma_d(R) = \Sigma_0 e^{-R/R_d}, \quad (4)$$

where Σ_0 is the central surface density, R_d is the scale length of the disk, and R is the distance from the centre of M31 in the plane of the disk. This corresponds to a disk mass within a sphere of radius r of

$$M_d(r) = 2\pi\Sigma_0 R_d^2 \left[1 - (1+r/R_d)e^{-r/R_d} \right]. \quad (5)$$

Here, $r = \sqrt{R^2 + z^2}$ is the distance from the centre of M31 and z is the distance perpendicular to the plane of the disk.

For an infinitesimally thin disk, Binney & Tremaine (1987) give the expression for the potential as:

$$\Phi_d(R, z) = -2\pi G\Sigma_0 R_d^2 \int_0^\infty \frac{J_0(kR)e^{-k|z|} dk}{[1+(kR_d)^2]^{3/2}}, \quad (6)$$

and in the plane of the disk, this thin disk potential implies a circular velocity profile given by (Binney & Tremaine 1987):

$$V_{c,d}^2(R) = 4\pi G\Sigma_0 R_d y^2 [I_0(y)K_0(y) - I_1(y)K_1(y)], \quad (7)$$

where $y = R/2R_d$ and (J_0 , I_0 , K_0 , I_1 , K_1) are Bessel functions.

Below, we shall also have occasion to use an extremely simple toy model that we will refer to as the ‘‘spherical disk’’ model. In this model, we assume that the disk mass within a sphere of radius r is distributed in a spherically symmetric fashion rather than concentrated in a thin disk. Then the corresponding gravitational potential is simply

$$\Phi_{d,sp}(r) = -2\pi G\Sigma_0 R_d^2 \left[\frac{1 - e^{-r/R_d}}{r} \right]. \quad (8)$$

Unless otherwise stated, the results presented in this paper will be based on the thin disk model.

2.4 The Extended Dark Halo

Finally, we consider the extended dark matter halo of M31. We assume that this component can be adequately modeled as a spherically symmetric system. We recognize that the issue concerning the sphericity of the halo is a contentious one, but given that it remains observationally unresolved even in the case of the Milky Way, we feel it more in keeping with the spirit of our approach to adopt the simplest model. To describe the run of density with radius, we adopt the NFW profile (Navarro, Frenk, & White 1996):

$$\rho_h(r) = \frac{\delta_c \rho_c}{(r/r_h)(1+r/r_h)^2}, \quad (9)$$

where $\rho_c = 277.72h^2 M_\odot/\text{kpc}^2$ is the present-day critical density, $h = 0.71$ is the Hubble constant in units of 100 km/s/Mpc, δ_c is a dimensionless density parameter, and r_h is the halo scale radius. N-body simulations based on the hierarchical clustering scenario for structure formation within the cold dark matter cosmogony suggest that spherically averaged halo density profiles are well described by the above profile. There is much debate over the exact exponent of the density in the inner cusp, but in our specific instance, this will not matter since the potential within the region in question will be dominated by the disk and/or the bulge components.

The mass profile and the corresponding potential for an NFW halo are given by:

$$M_h(r) = 4\pi\delta_c\rho_c r_h^3 \left[\ln\left(\frac{r+r_h}{r_h}\right) - \frac{r}{r+r_h} \right], \quad (10)$$

$$\Phi_h(r) = -4\pi G\delta_c\rho_c r_h^2 \left(\frac{r_h}{r} \right) \ln\left[\frac{r+r_h}{r_h} \right]. \quad (11)$$

3 SPECIFYING THE M31 MODEL PARAMETERS

The BH-Bulge-Disk-Halo mass model described above has a total of 6 structural parameters remaining to be specified: δ_c , r_h , M_b , r_b , Σ_0 , and R_d , or in other words a scale radius and normalization for each of the bulge, disk, and halo components. We constrain these parameters using a number of extant observations of M31.

Before discussing the data and our efforts to construct the mass model, we briefly review what is known about the configuration of M31. The Andromeda galaxy lies at a distance of 784 ± 24 kpc (Stanek & Garnavich 1998) from the Milky Way, and has a mean radial velocity of -300 ± 4 km/s (de Vaucouleurs et al. 1991). We look at the galaxy from below, as is evident from images of the disk dust lanes projected onto the bulge. We take the inclination to be 77° . This is the generally accepted value, although estimates range from 74° to 79° (Rubin & D’Odorico 1969; Waltherbos & Kennicutt 1988; Ma, Peng, & Gu 1997). The galaxy spins counterclockwise on the sky. We take the position angle of the disk to be 37° . The position angle of the bulge major axis appears to be offset from that of the disk by $\sim +10^\circ$ to $+20^\circ$ (McElroy 1983; Kormendy 1988) and additionally, the bulge isophotes have distinctly “box-shaped” appearances with ellipticities that increase with radius. These latter features, as well as the anomalously high non-circular gas velocities in the inner disk, have generally been interpreted as signatures of a triaxial bulge (Lindblad 1956; Stark 1977; Kent 1989; Stark & Binney 1994; Berman 2001; Berman & Loinard 2002). In addition, analyses of both the HI and the light distribution in M31 disk suggest that the disk is significantly warped, especially in the outer regions (cf. Sawa & Sofue 1982; Innanen, Kamper et al. 1982; Waltherbos & Kennicutt 1987, 1988; Morris, Reid, Griffiths & Penny 1994). Braun (1991) argues that in addition to this warping, the inclination of the M31 HI disk also varies as a function of both radius and azimuth and that it may even be flaring toward the outer regions. The latter is not altogether surprising in light of the number of satellites that appear to be interacting with the galaxy; the flaring of the disk is one of the generic features of such interactions (cf. Fardal, Babul & Barnes, in preparation).

Over the past two decades, detailed studies of M31 have generated a large volume of kinematic and photometric data. For practical considerations, we restrict ourselves to a limited number of data sets. Specifically, we constrain our mass model using both the M31 major-axis and average surface brightness profiles, the bulge major and minor axis velocity dispersion profiles, the disk rotation profile, and the dynamically derived total mass estimates in the intermediate and outer halo. These are described more fully in § 3.1–3.4. In order to relate our mass model to the light profiles, we are required to introduce two additional parameters: $(M/L_R)_b$ and $(M/L_R)_d$, or the mass-to-light ratios of the bulge and the disk. We assume that these two ratios are constant over the entire bulge and disk; this is probably not exactly correct but should be reasonably valid, given the modest color gradient in M31 (Waltherbos & Kennicutt 1987).

The inclusion of these mass-to-light ratios increases the number of parameters to 8. We tackle the problem of fitting these parameters in two steps. First, we fit the sur-

face brightness profile to obtain the scale radii r_b and R_d of the bulge and disk, and the luminosity normalization of these components. The abundance and quality of the surface brightness data is such that it would dominate the fit of the scale radii in any case. Also, the χ^2 from this fitting step is poor, which merely tells us that we have not managed to fit all the details of M31’s visual structure; in absolute terms, the size of the discrepancies is actually fairly small. Then, we incorporate the dynamical information to fit the four remaining parameters (the bulge and disk mass normalizations M_b and Σ_0 , and the two halo parameters r_h and δ_c). In contrast, the χ^2 from this fitting step is actually meaningful, and we use it to constrain the allowed region of parameter space.

We present the parameters for our best-fit solution in Table 2, and as we introduce below the set of observations that we use to constrain the model, we also describe how well our best-fit model fares in comparison. We defer until § 4 any discussion of errors, correlations, and possible degeneracies between the parameters, and the correspondence between the allowed terrain of parameter space and physical properties of M31.

3.1 M31 Surface Brightness Data

Given its proximity, M31 is one of the few galaxies visible to the naked eyes. Its existence was first documented by the Persian astronomer Abd al-Rahman Al-Sufi in his treatise on stellar astronomy titled “Kitab al-Kawatib al-Thabit al-Musawwar” (Book on the Constellations of the Fixed Stars), published in AD 964, where he both identified its position in the sky and summarized his observations. Though subject of some speculation and study over much of the ensuing millennium, it was Hubble’s epochal study (Hubble 1929) establishing the true nature of M31 as an extragalactic stellar system (galaxy) that underlies the considerable effort devoted to the study of M31 since the 1930s. As a result, there is no dearth of high resolution photometric data on the system. Here, we will use both the azimuthally-averaged (or “global”) surface brightness profile and the major-axis profile to constrain our models. The global profile has the advantage of minimizing effects from localized structural features, like the spiral arms, which can introduce bumps and wiggles in the light curve along any one direction. In the left panel of Figure 1, we plot the *R*-band global light profile of Waltherbos & Kennicutt (1987). We use the *R*-band profile because we expect it to be less affected by dust extinction and stellar population variations than bluer bands. For reasons discussed below, we find it necessary to shift the Waltherbos & Kennicutt (1987) major axis surface brightness profile by -0.1 mag, and since the major axis and the present global light profiles are derived from the same photographic plates, we apply the same shift to the global profile as well. Waltherbos & Kennicutt compute the mean surface brightness at radial coordinate r by averaging the light in an elliptical annulus formed by taking a face-on circular ring of radius r and thickness δr , rotating it to an inclination of 77° , projecting the resulting structure onto the plane of the sky, and aligning the major axis of the resulting elliptical annulus with the major axis of M31. When we compute the global surface brightness for our model, we follow the same procedure.

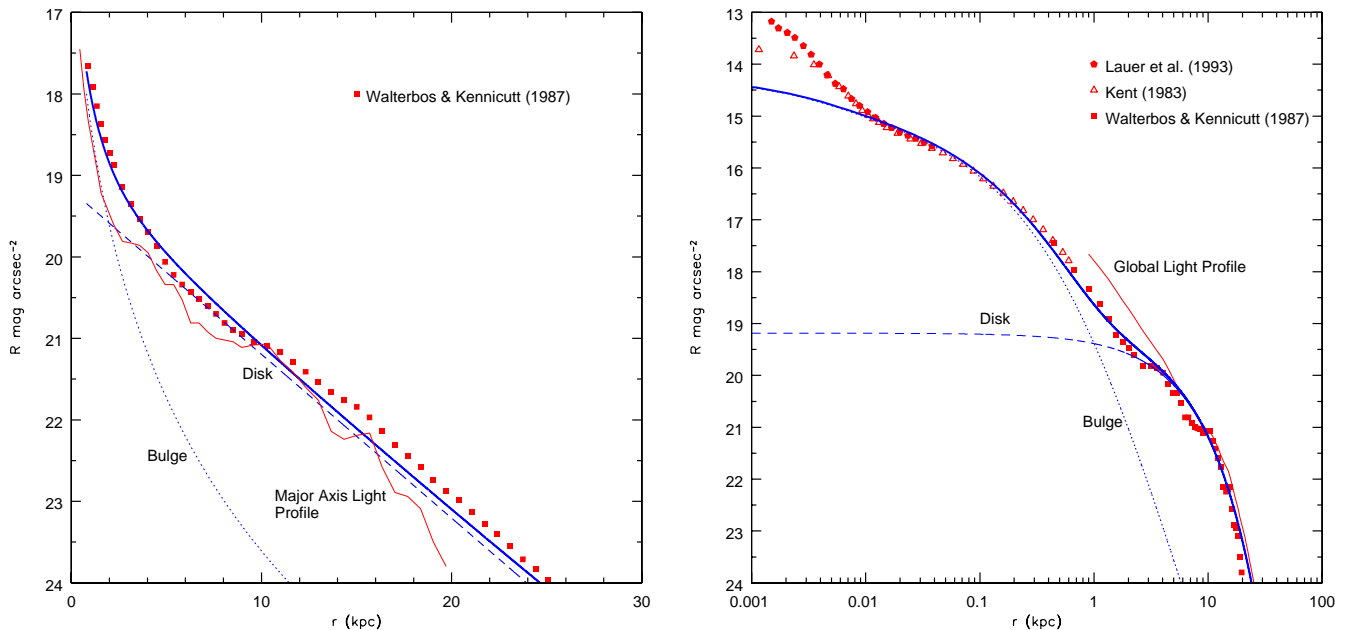


Figure 1. Left panel: The global surface brightness profile of M31 in log-linear projection. The red squares represent the data of Walterbos & Kennicutt (1987), corrected as described in the text. The blue lines show the results of our best-fit model. The dotted line is the bulge contribution, the dashed line the disk and the thick solid blue line is the total. For comparison purposes, we juxtapose the observed major axis surface brightness data of Walterbos & Kennicutt (1987) from the right panel as the thin red line. Right panel: The symbols trace the composite, observed M31 major axis surface brightness profile in log-log projection. For comparison, we plot the observed global light from the left panel as a thin red line. As in the left panel, the blue lines represent the major axis light profile for our best-fit model.

The Walterbos & Kennicutt (1987) global light profile only extends down to just under 1 kpc along the major axis, and therefore just begins to probe the region where the light is dominated by the bulge. On the other hand, there have been a number of studies of the light profile along the major axis that probe all the way in to the very central nuclear region. We, therefore, also include the major-axis profile among our set of constraints. We plot this profile in the right panel of Figure 1. This combines the nuclear region *HST* data from Lauer et al. (1993), intermediate radii data from Kent (1983), and large radii data from Walterbos & Kennicutt (1987). To convert Kent’s r -band data and Lauer et al.’s V -band data into an R -band light profile, we use colours $V - R \approx 0.75$ (Tenjes et al. 1994) and $r - R \approx 0.35$ (Jorgensen 1994). As a check, we have tested these color transformations by running a stellar burst model in the PEGASE.2 population synthesis code (Fioc & Rocca-Volmerange 1997). For a burst time of 12 Gyr, we find agreement within ± 0.1 mag between our adopted offsets between V , r and R , as well as other measured colours of M31’s bulge presented in Table 1. Additionally, we found it necessary to translate the Walterbos & Kennicutt (1987) data by -0.1 mag in order to bring it in line with the other two data sets. This level of fine-tuning is not surprising given an uncertainty of ~ 0.1 mag in the colours as well as ~ 0.1 mag zero-point errors in the surface brightness measurements.

The major-axis light profile strongly indicates that the stellar nucleus ($r < 0.01$ kpc) and the bulge are two separate components (see also Kormendy & Bender 1999). As

noted previously, we do not attempt to model the nucleus because its mass is too small to affect the masses of our galaxy components or orbits in the halo region. The major-axis profile also has a series of prominent bumps not present in the global light curve, due to dust lanes, disk warps, and spiral arms that intersect the major axis. Azimuthal averaging minimizes the presence of such features in the global profile.

We compute the model major-axis surface brightness profile as $\mu(r) = \mu_b(0.9r) + \mu_d(r)$, where the disk and bulge surface brightness profiles in the R -band are given by

$$\mu_d(r) = \left(\frac{M}{L_R}\right)_d^{-1} \Sigma_0 e^{-r/R_d} \sec(i), \quad (12)$$

$$\mu_b(r) = 2 \left(\frac{M}{L_R}\right)_b^{-1} \int_r^\infty \rho_b(x) \frac{x}{\sqrt{x^2 - r^2}} dx. \quad (13)$$

Notice that in computing the surface brightness at projected distance r along the major axis, we sum the disk surface brightness at that projected distance with the bulge surface brightness at $0.9r$. We do so in order to compensate for the fact that in our model the light distribution is circularly symmetric while the observed light distribution is ellipsoidal. The factor 0.9 comes from our requiring that the area enclosed by an elliptical isophote at distance r along the major axis is the same as the area of our equivalent circle. This “correction” results in our circularly symmetric bulge light profile being stretched outward.

When fitting the major axis and the azimuthally-averaged surface brightness data, we assign an uncertainty of ± 0.1 mag arcsec $^{-2}$ to each data point. The random er-

Table 1. Observed M31 Bulge Colors

Bulge Color	Reference
$r - R \approx 0.35$	(Jorgensen 1994)
$B - r \approx 1.28$	(Kent 1987)
$V - R \approx 0.75$	(Tenjes et al. 1994)
$B - R \approx 1.7$	(Walterbos & Kennicutt 1987)
$B - V \approx 0.97$	(Walterbos & Kennicutt 1987; Tenjes et al. 1994)
$V - K \approx 3.38$	(Pritchet 1977)
$V - I \approx 1.34$	(Lauer et al. 1993)
$g - r \approx 0.55$	(Hoessel & Melnick 1980)
$v - g \approx 0.78$	(Hoessel & Melnick 1980)

* All colors have an uncertainty of ± 0.1

rors are probably a strong function of radius since they drop with surface brightness, but there are significant systematic errors from zero-point shifts and color correction terms in all parts of these diagrams (Walterbos & Kennicutt 1987).

Furthermore, there are many features that cannot be fit using our simple model, and some of these are primarily features in the luminosity (e.g., dust lanes) and not in the mass. Our goal is simply to get a close approximation to the surface brightness at all radii, not to follow every feature. To this end, we use a standard χ^2 fitting routine to obtain the best-fit parameters, but ignore the actual value of χ^2 which indicates a poor fit (reduced χ^2 is about 7).

The two panels of Figure 1 show the global and major axis light profiles for our best-fit mass model for M31. Over most of the region of interest, the model agrees with the data within 0.2 mag. At first glance, the systematic offset of ~ 0.2 mag at $r > 10$ kpc between the model and the data global surface brightness profiles may seem disconcerting. This offset is due to the fact that for $r > 10$ kpc, the *observed* global light profile is brighter than the major-axis profile by as much as 0.5 mag at $r = 20$ kpc (Walterbos & Kennicutt 1987). To facilitate comparison, we show the trace of the observed major-axis and the global light profiles in the left and right panels of Figure 1, respectively. If the disk was indeed an infinitesimally thin, perfectly axisymmetric system and the bulge truly spherically symmetric, the major-axis and the global light profiles of the disk would be indistinguishable. The observed differences in the light profiles are due to the increased contribution to the global light profile by the bulge due to its ellipsoidal shape, the warpage in the disk, and its finite thickness. Since our mass model does not include these additional features, we do not expect to be able to model the offset. Instead, our best-fit model “splits the difference” and settles in between the two.

3.2 Disk Rotation Curve

Figure 2 shows the rotation profile of the M31 disk. As with the photometric data, there is no dearth of optical and radio observations of the rotation data for the M31 disk. We use the smoothed, composite rotation curve of Widrow, Perrett, & Suyu (2003), which was based on the HII emission region observations of Kent (1989) and the HI measurements of Braun (1991).

The two left panels and the top right panel of Figure 2 also show the total disk rotation curve of our best-fit model (thick solid curve), along with the contributions from the bulge, disk and halo components (thick dotted, thick dashed

and thick dot-dashed curves, respectively). Our model results are in excellent agreement with the observations and we remind the reader that the corresponding model parameters are listed in Table 2.

In the top left panel, we also show the results of a model that we have dubbed the “spherical disk” model. The halo and the bulge components in this model are exactly the same as in the best-fit axisymmetric model. In fact, even the total radial mass profile for the disk component, $M_d(< r)$ is the same in the two cases. In the spherical disk case, however, this mass is assumed to be distributed in a spherically symmetric fashion, as opposed to planar and axisymmetric. As Figure 2 illustrates, the rotation profiles for the two models (and hence, the potential, at least in the plane of the disk of the axisymmetric case) are similar with minor differences being solely due to the different geometries of the disk mass distribution. Since orbit calculations in purely spherical potentials are much faster to compute, we use the spherical disk model to narrow the space of potentially acceptable satellite orbits and then, use the axisymmetric model to explore this limited space further. This latter step is necessary because as we demonstrate in §4.2, the nature of the disk potential, whether axisymmetric or spherically symmetric, impacts the satellite orbits in non-trivial ways.

In the bottom left panel, we juxtapose our best-fit axisymmetric model against the results for a model where the disk mass-to-light ratio has been constrained to be $M/L_R = 3.3$, which is lower than the mass-to-light ratio of the disk in the best-fit case. In the top right panel, we juxtapose our best fit-axisymmetric model against the results for a model, which we will refer to as the “maximum disk” model, where the disk mass-to-light ratio has been constrained to be $M/L_R = 6.3$, a value that is much higher than the M/L of the disk in the best-fit case. The parameters for the two constrained models are also given in Table 2, and reasons for considering these two additional models are discussed in §4.1. Here, we merely note that total rotation profiles for the formal best-fit model, the constrained- M/L model and the maximum disk model are virtually indistinguishable. Fixing the disk mass-to-light ratio forces the disk mass higher or lower relative to the best-fit model. The corresponding change in the disk contribution to the total rotation profile is entirely compensated by an opposite change in the halo contribution. This payoff between the disk and the halo is an example of the degeneracy that, in the absence of any additional constraints, is a fundamental source of uncertainty affecting all efforts to construct mass models of disk galaxies. We discuss the nature of, as well as our efforts to break this degeneracy in §4.1.

3.3 Bulge Velocity Dispersion

In Figure 3, we show the projected bulge velocity dispersion profile along the bulge major (PA=45°–55°) and minor (PA=135°–160°) axes. The former is plotted in the upper panel while the latter is shown in the lower panel. The filled data points (circles) with error bars show the observed dispersion that we are using in our fitting procedure. These correspond to the measurements by Kormendy (1988) along PA=55° (major) and PA=160° (minor). We only consider measurements at $r \gtrsim 0.02$ kpc to avoid complications due to the BH.

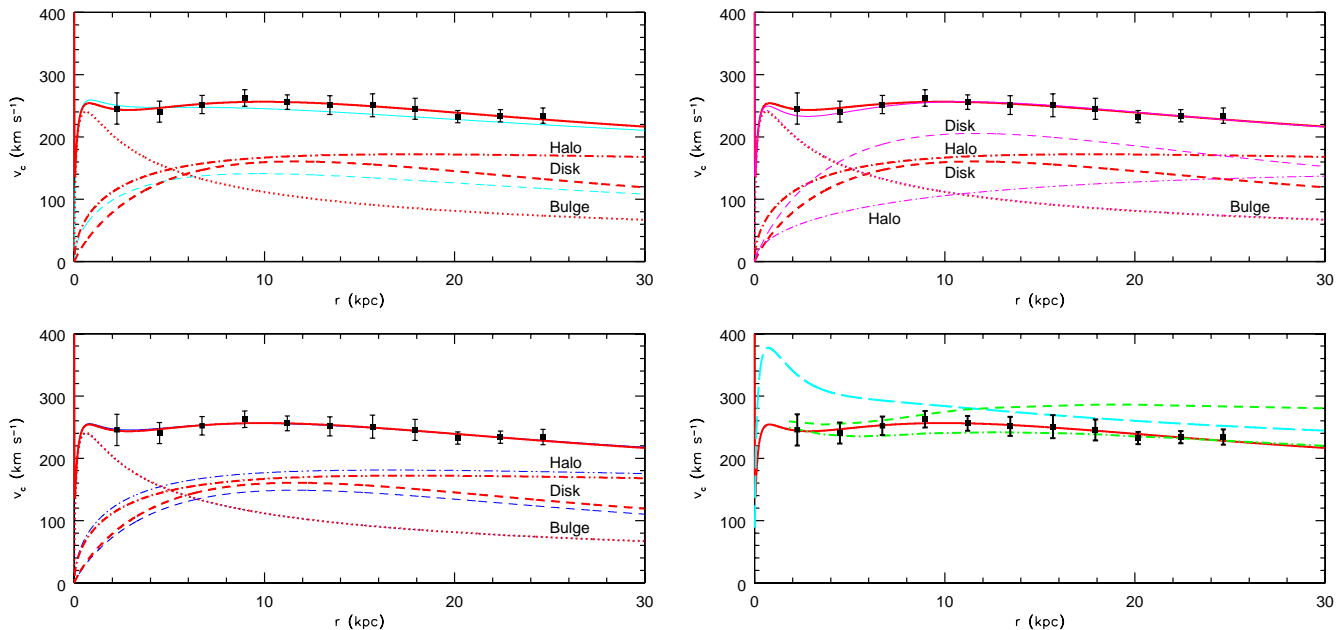


Figure 2. The top left panel shows our best-fit axisymmetric (thick red lines) and spherical disk (thin cyan lines) model rotation curves, in comparison to the M31 disk rotation profile. The solid curves show the total model rotation curves. The short dashed lines show the contribution to the total from the disk, the dotted lines, from the bulge, and the dot-short dashed lines, from the halo. The spike in the curves at $r = 0$ is due to the presence of the BH. The bottom left panel compares the best-fit axisymmetric and constrained ($M/L=3.3$) disk models. As in the top panel, the thick red lines correspond to the best-fit axisymmetric model. The thin blue lines show the results for the $M/L=3.3$ model. The line types are the same as in the top panel. The top right panel compares the best-fit axisymmetric (thick red lines) and the maximum disk (thin magenta lines) models. Line types are the same as discussed above. The bottom right panel compares our best-fit model rotation curve (thick red lines) against those of recently used models: the Bekki et al. (2001) model used by Font et al. (cyan long-dashed line), as well as the high (green short dashed line) and the low (green dot-dashed line) Klypin, Zhao, & Somerville (2002) models used by Ibata et al.

For comparative purposes only, we also include on the plot data points from Kormendy (1988) taken along $PA=38^\circ$ (open circles) as well as the data from Kormendy & Bender (1999) (open triangles). The latter extends the velocity dispersion profiles well into the nucleus of M31 and the trend in the measurements towards smaller radii reflects the increasing gravity due to the BH. Focusing on the $PA=38^\circ$ data from Kormendy (1988) (open circles), we note that this latter set is indistinguishable from that for $PA=55^\circ$ in the region of overlap, suggesting that small variations in the position angles along which the measurements are made or the fact that these measurements may not be mapping out the velocity dispersion profile precisely along the “true” bulge major axis does not appear to introduce any significant biases.

For completeness, we also show the data points (open squares) corresponding to the smoothed profile of Widrow, Perrett, & Suyu (2003), which itself is based on data from McElroy (1983). We only show the data only out to 1 kpc, since beyond this point we are concerned about the dynamical effect of bulge rotation and/or contamination from the disk. There is one aspect of this data set that is slightly disconcerting. In the region of overlap along the major axis, the Kormendy (1988) data implies $\sim 15\%$ higher velocity dispersion than the McElroy (1983) observations. We do not understand the origin of this disagreement.

The solid curves in the two panels show the velocity

dispersion for our best-fit mass model. The results match fairly well to the data points actually used to constrain our model. In keeping with the observations, the model profiles decline towards increasing radii beyond $r = 0.2$ kpc though the decline is not as steep as indicated by McElroy (1983). Moreover, although the model was not constrained to fit the Kormendy & Bender (1999) data, it nonetheless reproduces the gentle decline towards the center inward of 0.1 kpc, the trough at ~ 0.01 kpc, and the subsequent rise into the center.

In computing the model velocity dispersions, we have made three additional simplifications, in keeping with our basic assumption of a spherically symmetric bulge. These additional assumptions are: (a) The bulge velocity dispersion is isotropic; (b) the disk potential in the central 1.2 kpc can be approximated by that of the spherical disk; and (c) the bulge rotation can be neglected. Then the true (unprojected) bulge velocity dispersion is

$$\sigma_r^2 = \frac{1}{\rho_b(r)} \int_r^\infty \rho_b(r') \frac{\partial \Phi_{tot}}{\partial r'} dr'. \quad (14)$$

The observations, however, yield the luminosity-weighted *projected* velocity dispersion. The equivalent model profile is (Simien, Pellet, & Monnet 1979; Kent 1989)

$$\sigma_p^2(r) = \frac{1}{\mu_b(r)} \left(\frac{M}{L_R} \right)_b^{-1} \int_r^\infty \rho_b(r') \sigma_r^2(r') \frac{r'}{\sqrt{r'^2 - r^2}} dr', \quad (15)$$

where $\mu_b(r)$ is the bulge surface brightness profile given in

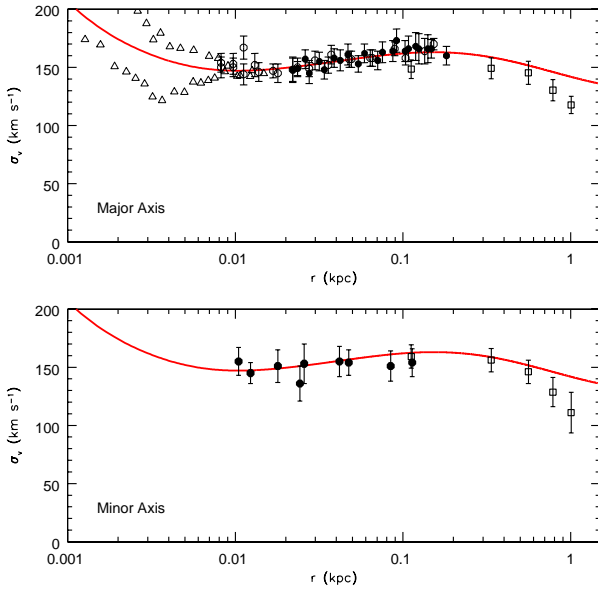


Figure 3. The upper and lower panels show the measured bulge velocity dispersion along the bulge major and minor axis, respectively. The solid curve represents our best-fit model. The filled circles represent data of Kormendy (1988) along PA=55° (upper panel) and along PA=160° (lower panel). Also plotted are the major and minor axis velocity dispersion data of McElroy (1983) as smoothed by Widrow, Perrett, & Suyu (2003) (open squares), the major axis data of Kormendy & Bender (1999) (open triangles), and the major axis data of Kormendy (1988) along PA=38° (open circles). The upturn in the curves at ~ 0.01 kpc is due to the influence of the central BH.

(13). Since the projected velocity dispersion is luminosity-weighted and since our model isophotes are circular whereas the actual bulge isophotes are elliptical, it would seem that we perhaps ought to rescale our profiles so that along the major axis, $\sigma_p(r)$ is stretched out by $\sim 10\%$ and along the minor axis, $\sigma_p(r)$ compressed by the same amount. However, we omit this step, since $\sigma_p(r)$ is so flat that this rescaling has a negligible effect.

After comparing our results to those obtained with more sophisticated assumptions about the bulge geometry and velocity distribution, we find that the three assumptions listed above, especially assumptions (b) and (c), do not appear to affect our results significantly. We base this assertion on the discussion in Simien, Pellet, & Monnet (1979) and Kent (1989). The former, for example, demonstrate that impact of rotation on the determination of $\sigma_p^2(r)$ is negligible for $r < 0.3$ kpc. Between 0.3 and 1.0 kpc, the bulge rotation profile rises from $V_{c,b} \sim 0.3\sigma_p$ to $0.5\sigma_p$. It might be thought that this increases the support from rotation and induces the slight discrepancy between our models and the data at ~ 1 kpc. As reasonable as this sounds, the argument is not supported by the results of Kent (1989). In constructing his mass model, Kent assumed, like us, an isotropic bulge velocity dispersion but, unlike us, he also used an oblate spheroidal model for the mass distribution of the M31 bulge, explicitly took into account the axisymmetric nature of the disk potential, and allowed for bulge rotation. Kent’s velocity dispersion profiles are, however, similar to ours both in

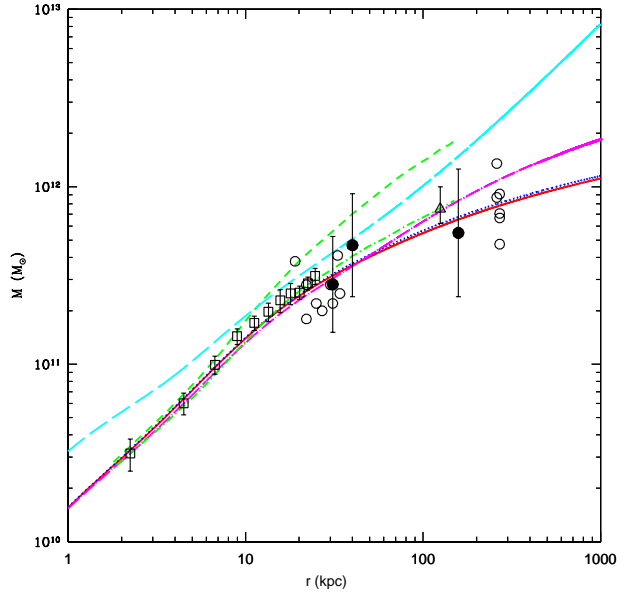


Figure 4. A comparison of the mass profiles for different models: our formal best-fit model (solid red line), our best-fit models for $(M/L_R)_d=3.3$ (dotted blue line) and the maximum disk (dot-long dashed magenta line), the two axisymmetric models of Ibata et al. based on the mass models of Klypin, Zhao, & Somerville (2002) (the dashed and dot-dashed green lines), as well as the bulge-disk-halo model of Bekki et al. (2001) used by Font et al. (long dashed cyan line). The solid circles represent mass estimates made by Evans et al. (2000) and Evans & Wilkinson (2000) that we used as constraints on our mass models. The first two solid circles are mass estimates from planetary nebula and globular cluster tracers, respectively, from Evans & Wilkinson (2000). The last solid circle is a mass estimate based on M31 satellite galaxies from Evans et al. (2000). The open squares represent the mass estimate based on the observed rotation profile computed using the spherical approximation. The open triangle represents an estimate of the mass within 125 kpc derived by Ibata et al. (2004) while the open circles represent mass estimates from many sources which are summarized in Table 6 of Evans & Wilkinson (2000). None of the mass estimates shown as open symbols were used as constraints on our mass model.

shape and magnitude. In particular, the Kent model profiles also do not fall off as rapidly as the observed profile. To the extent that we have an excellent overall agreement with the more rigorous calculations of Kent (1989), we feel justified in having made our simplifying assumptions. A clue to the origin of the steeper than predicted decline in $\sigma_p^2(r)$ may lie in the different rates at which the major and minor axis profiles fall off. Both Simien, Pellet, & Monnet (1979) and Kent (1989) note these differences may be indicative of velocity anisotropy.

We note that our neglect of bulge rotation is primarily motivated by consistency with our assumption of a spherical bulge, and by its small level relative to the bulge velocity dispersion. Additionally, McElroy (1983) noted several asymmetries in the rotation curves on the two sides of the putative axis of rotation as well as along various different position angles. This suggests the determination of a mean bulge rotation velocity is not straightforward, which also encourages us to neglect it.

3.4 Total Mass Estimates from the Intermediate and Outer Halo Regions

Finally, we consider the constraints on the total mass of the system from dynamical studies of globular clusters, planetary nebulae and M31 satellites. A number of researchers have used these tracers to estimate the total mass profile of M31 in the intermediate and the outer regions of the halo. However, few of these estimates contain a well-motivated error bar, which we need for our fitting procedure; many authors simply propagate the observational errors through their mass estimator and ignore the larger statistical errors altogether. For the present purposes, we thus use the results of Evans & Wilkinson (2000) and Evans et al. (2000), who estimate the errors using Bayesian statistics. Using the planetary nebulae and globular cluster data, Evans & Wilkinson (2000) estimate that $M(< 31 \text{ kpc}) = (2.8_{-1.2}^{+2.4}) \times 10^{11} \text{ M}_{\odot}$ and $M(< 40 \text{ kpc}) = (4.7_{-2.3}^{+3.4}) \times 10^{11} \text{ M}_{\odot}$, respectively. Of these two, Evans & Wilkinson (2000) argue that the mass estimate based on globular clusters is more robust because these tracers are more uniformly distributed while the planetary nebulae tend to be concentrated in two regions near the optical disk. To estimate the mass further out in the halo, Evans et al. (2000) analyzed the data for the satellite galaxies of M31, including the spiral galaxy M33. We use their results to estimate the mass at 158 kpc, which is the radius of the median object (And II) in the sample of 13 M31 satellites, *excluding* Pegasus and IC 1613. These two satellites appear to be outside M31's virial radius and thus are not appropriate to include in an analysis that assumes statistical equilibrium. We obtain the mass estimate by averaging the results of their two velocity distributions, and making a small correction from their stated total mass to $M(< 158 \text{ kpc})$ using their mass profile. This gives $M(< 158 \text{ kpc}) = 5.5_{-3.1}^{+7.1} \times 10^{11} \text{ M}_{\odot}$. For each of the three halo mass estimates, we convert the given confidence intervals to symmetrical error bars in $\log(M)$ for use in our χ^2 fit.

In Figure 4, we show the above three mass estimates as filled circles. These are the values that we use to constrain our mass models. For illustrative purposes, however, we also plot a number of other mass estimates. The open squares extending from ~ 2 to $\sim 30 \text{ kpc}$ trace the mass estimates based on the rotational curve data, computed using the spherical approximation $V_c^2 = GM/r$. The open triangle at 125 kpc designates the mass estimate derived by Ibata et al. (2004) from their preliminary analyses of the dynamics of the giant southern stream. We shall consider this further in Paper II. Finally, the open circles represent mass estimates by a number of different researchers, taken from Table 6 of Evans & Wilkinson (2000).

Figure 4 also shows the results of our best-fit model (solid red curve) and two variants, one with the disk mass-to-light ratio fixed to $(M/L_R)_d=3.3$ (dotted blue line) and the maximum disk model (dot-long dashed magenta line). All three curves are in excellent agreement with not only the three data points used as constraints, but also in good agreement with the entire slew of mass estimates shown in the figure. The curves, however, do lie systematically below the mass estimates computed from the observed rotation profile using the spherical approximation. Since the rotation curve associated with these models are in excellent agreement with the observed profile, this comparison shows clearly the effect

of neglecting disk flattening. The virial mass (M_{200}) corresponding to the three axisymmetric models spans the range $6.8\text{--}9.4 \times 10^{11} \text{ M}_{\odot}$ (see Table 2).

4 PROPERTIES OF ALLOWED MODELS

The parameters corresponding to our formal best-fit mass model for M31 are listed in Table 2. The table also shows parameters corresponding to two alternatives to our formal best-fit model, one where the disk mass-to-light is fixed to $(M/L_R)_d=3.3$ and another where the disk mass is fixed to the maximum allowed value. We discuss below the reasons for considering these alternative solutions.

4.1 Allowed Region of Parameter Space

In general, attempts to model the mass distribution in galaxies are hampered by degeneracies between the various parameters. In our specific case, we had expected to encounter a linked bulge-disk-halo degeneracy where the halo and the disk played off against each other to match the M31 rotation profile, while the disk and the bulge did the same with respect to the inner region dynamics. In fact, our combined use of photometric and kinematic data sets greatly reduces the available degrees of freedom.

Of the 8 parameters, two — the disk and bulge mass-to-light ratios — are not really independent variables. They appear in Equations (12) and (13) as multiplicative factors relating disk and bulge mass profiles to the M31 light profiles. Consequently, once the disk parameters (Σ_0, R_d) are determined, the M31 surface brightness profiles fix the disk mass-to-light ratio to high accuracy. The same is true of the bulge. The light profiles also determine the bulge and disk scale radii fairly precisely to 0.61 ± 0.10 and $5.40 \pm 0.13 \text{ kpc}$, respectively. We therefore fix r_b and R_d to these values after doing the surface brightness fit, removing these particular degrees of freedom entirely. To estimate the errors, we have adopted the approach advocated by Press et al. (2001) and rescaled the error estimate associated with individual data points such that the effective reduced χ^2 is unity. As noted in §3.1, our fit to the M31's light profile is poor in a formal sense using the original photometric errors (the corresponding reduced χ^2 is 7) because we do not attempt to fit the various visual features present therein. By increasing the error bars, we are effectively rendering the physical variations in the light curves due to dust lanes, disk warps and spiral arms statistically insignificant. We then use this rescaled χ^2 to approximate the uncertainties in the bulge and disk scale radii estimates.

Additionally, we find that the two halo parameters δ_c and r_h are coupled so strongly that if all other parameters are already fixed, setting one effectively sets the other. The main reason for this is the small error bars on the rotation curve points, which put tight constraints on the halo contribution there. The constraints on the outer halo force are not as strong, as can be seen in Figure 4.

Moreover, the solutions with the lowest χ^2 lie on a thin plane corresponding to a specific set of bulge masses M_b . The values of this parameter are remarkably robust in that forcing large changes in the values of the other parameters result in changes of $< 10\%$. This was previously noted by

Table 2. M31 Mass Model Parameters for Best-fit, disk with $(M/L_R)_d=3.3$, and Maximum disk cases

Parameter	Symbol		Best-fit Model	$(M/L_R)_d=3.3$	Maximum Disk
Black Hole Mass	M_\bullet	$(10^7 M_\odot)$	5.6	5.6	5.6
Total Bulge Mass	M_b	$(10^{10} M_\odot)$	3.3	3.2	3.3
Total Disk Mass	M_d	$(10^{10} M_\odot)$	8.4	7.2	13.7
Total Mass inside 125 kpc	$M(< 125 \text{ kpc})$	$(10^{11} M_\odot)$	5.6	6.2	7.3
Virial Mass	M_{200}^*	$(10^{11} M_\odot)$	6.8	7.1	9.4
	M_{100}^*	$(10^{11} M_\odot)$	7.5	7.7	10.8
Bulge Scale Radius	R_b	(kpc)	0.61	0.61	0.61
Disk Scale Radius	R_d	(kpc)	5.4	5.4	5.4
Halo Scale Radius	r_h	(kpc)	8.18	7.63	28.73
Virial Radius	R_{200}^*	(kpc)	180.0	182.3	200.3
	R_{100}^*	(kpc)	231.8	234.8	262.4
Halo Density Parameter	δ_c	(10^4)	27.0	34.4	1.54
Halo Concentration Parameter	$C_{200} \equiv R_{200}/r_h$		22.0	23.9	7.0
Bulge M/L	$(M/L_R)_b^{**}$		3.9	3.9	4.0
Disk M/L	$(M/L_R)_d^{**}$		3.9	3.3	6.3
Disk Central Surface Density	Σ_0	$(10^8 M_\odot/\text{kpc}^2)$	4.6	3.9	7.5
Maximum Rotation Velocity	$V_{c,max}$	km/s	256.5	255.9	256.5
Fraction of “galactic” baryons	$\Omega_m(M_b + M_d)/(\Omega_b M_{200})$		0.99	0.86	1.0

* We define M_Δ as the mass enclosed with the sphere of radius R_Δ such that the mean density inside is $\Delta\rho_c$, where $\Delta = 100$ or 200 and $\rho_c = 277.72h^2 M_\odot/\text{kpc}^2$ is the present-day critical density.

** The quoted M/L ratios are based on luminosities that have *not* been corrected for internal or foreground extinction.

Widrow, Perrett, & Suyu (2003), who described the neighbourhood of their best-fit solution as a “trough [in the M_d – M_b plane] running parallel to the M_d axis.”

This then leaves just two parameters, Σ_0 and one of the two halo parameters, to span most of the available parameter space. In Figure 5, we show the location of our formal best-fit solution and the corresponding χ^2 contours in the Σ_0 – r_h plane. Here we show contour levels of $\Delta\chi^2 \equiv \chi^2 - \chi^2_{\min} = 1.0, 2.7, \text{ and } 4.0$, corresponding to 68%, 90% and 95% confidence intervals in the case of one parameter, and 39%, 74%, and 86% in the case of two parameters (Press et al. 2001). (Initially we regard both parameters as free, but later we will assume a value for the disk M/L , resulting in just one free parameter.) This plot shows that there is a huge area of the plane that produces acceptable fits, although the transverse width of this allowed region in the remaining dimensions of parameter space is rather small. The importance of the formal best-fit solution is thus diluted by this large allowed volume, and it is worth seeing whether we can put any more constraints on the family of solutions as a whole.

In the upper panel, we superpose on the contour map lines of constant total mass within 125 kpc. The shape of the contours shows that the main degeneracy is the tradeoff between the disk and halo components; this is not very surprising, as this tradeoff is a long-standing problem in fitting galaxy rotation curves (Dutton et al. 2005). The allowed region extends from “maximum disk” models at the upper right, to models where the disk is a minor contributor to the rotation curve at the lower left. The extension in the other direction, across the mass contours, is due to the large uncertainty in the outer halo mass, which allows for a large tradeoff between r_h and δ_c .

The best-fit solution lies on the line for $M(< 125 \text{ kpc}) =$

$6.1 \times 10^{11} M_\odot$. As already noted, Ibata et al. (2004) have carried out a preliminary analysis of the dynamics of the giant southern stream, a separate constraint to those examined here, and their results require that $M(< 125 \text{ kpc}) > 5.4 \times 10^{11} M_\odot$. This constraint reduces the region of allowed parameter space by excluding the lower right corner region of the $\Delta\chi^2 = 4.0$ confidence region, along with the entire lower right quarter of the Σ_0 – r_h plane.

In the middle panel of Figure 5, we superpose lines of constant halo concentration C_{200} on the contour map. (Our notation emphasizes we use the radius enclosing a mean density of 200 times the critical density to define the virial radius and concentration, in contrast to some other authors.) Numerical simulation studies suggest that in the absence of baryons, the concentration parameters of $\sim 10^{12} M_\odot$ halos are in the range $C_{200} \approx 7$ – 14 (Bullock et al. 2001; Wechsler et al. 2002; Dolag et al. 2004). If anything, the inclusion of baryons ought to make the halos more concentrated due to gravitational compression of the inner regions of the halo, following the expected cooling and pooling of the baryons at the centre of the halos (Blumenthal, Faber, Flores, & Primack 1986; Klypin, Zhao, & Somerville 2002). On the other hand, heating of the dark matter by gas clumps during galaxy formation (Mo & Mao 2004) and by a bar in the central disk (Weinberg & Katz 2002) may partially counteract this effect. For these reasons, we use $C_{200} > 7$ as a lower limit on the effective dark halo concentration. This condition excludes the upper third of the Σ_0 – r_h plane, including some of the $\Delta\chi^2 = 4.0$ confidence region.

Finally, the lower panel superposes the contours of the fraction of baryons within the virial radius R_{200} that are “galactic”, i.e., within the bulge or the disk component:

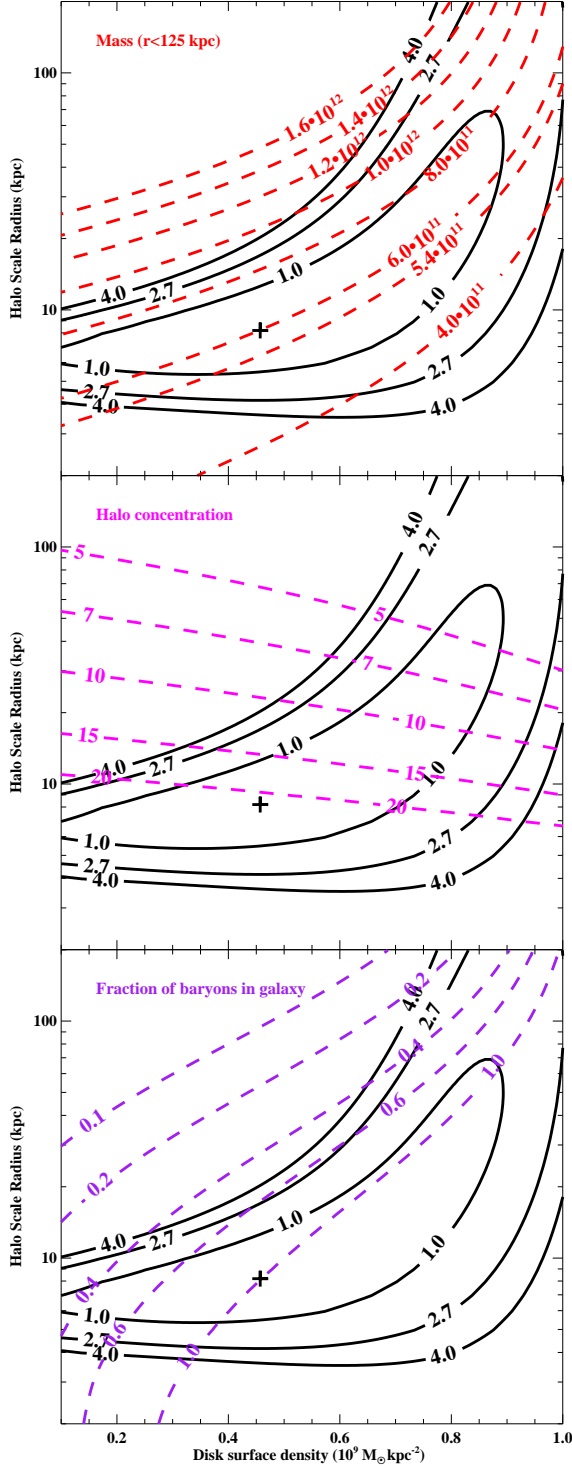


Figure 5. The cross in the above three panels marks the location of the formal best-fit solution (see Table 2), and the solid black curves show the corresponding $\Delta\chi^2 = 1.0, 2.7, 4.0$ contours. The upper panel superposes the contours corresponding to constant total mass within 125 kpc (red dashed lines); the middle panel shows lines of constant halo concentration C_{200} (magenta dashed lines); and the lower panel shows lines of constant baryon fraction (purple dashed lines) as defined in the text.

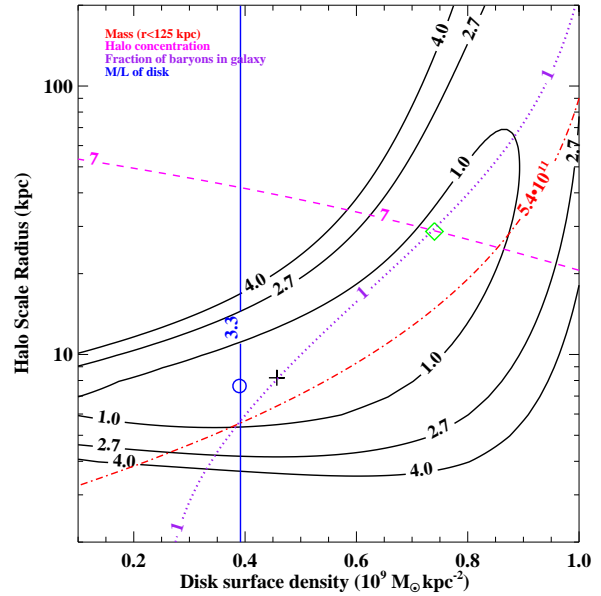


Figure 6. The above plot again shows our formal best-fit model (cross) and the $\Delta\chi^2 = 1.0, 2.7, 4.0$ contours (black solid lines). However, we have also combined, for clarity, the three critical demarcations from the panels in Figure 5 (see text). We assert that the allowed region for physically plausible solutions is the section of the $\Delta\chi^2 < 4.0$ region that is bounded at the top by $C_{200} = 7$ (magenta dashed curve) and to the right by $f_{\text{gal}} = 1$ (purple dotted line). Additional lines on the plot correspond to $M(< 125 \text{ kpc}) = 5.4 \times 10^{11} M_{\odot}$ (red dot-dashed curve) and disk mass-to-light ratio (uncorrected for extinction) of $(M/L_R)_d = 3.3$ (solid blue vertical line). Our constrained, best-fit, physically plausible solution is shown as an open circle on the $(M/L_R)_d = 3.3$ line. Our constrained, maximum-disk solution is shown by the green diamond.

$f_{\text{gal}} = \Omega_m(M_d + M_b)/(\Omega_b M_{200})$. In computing this quantity, we assume that the bulge and the disk are purely baryonic. This is a long-debated assumption even in the case of the Milky Way, but the disk and bulge are probably not *dominated* by dark matter so that the error from this assumption is probably small. Since f_{gal} must be less than unity, much of the lower right half of the Σ_0 - r_h plane is excluded. For $\Sigma_0 > 4.5 \times 10^8 M_{\odot}/\text{kpc}^2$, this condition is stricter than that of $M(< 125 \text{ kpc})$. Figure 6 shows all three constraints on a single plot. These constraints, in combination with the $\Delta\chi^2$ contours, severely restrict the region of allowed solutions.

The uncorrected disk mass-to-light ratio of our formal best-fit solution is $(M/L_R)_d = 3.9$, which is a bit on the high side. The mean luminosity-weighted $B - R$ color of M31's disk is $B - R \approx 1.60$ (Walterbos & Kennicutt 1987). Using the color- M/L relations of Bell & de Jong (2001), this corresponds to a mass-to-light ratio of $M/L_R \approx 3.5$. Admittedly, the above $B - R$ color is uncorrected for reddening due to dust while the Bell & de Jong (2001) relations are for dust-free quantities. However as they note, the very dust that is responsible for the reddening also extinguishes the light from the galaxy, increasing the M/L ratio, and to first order the two effects cancel out. A more careful analysis suggests that the M/L derived using uncorrected colors can be an overestimate by as much as ~ 0.1 dex. We therefore adopt a

value of $M/L_R \approx 3.3$ (uncorrected) for the M31 disk, though we recognize that this ratio could be as low as 2.8.

We can also estimate the corrected or true mass-to-light ratio for the M31 disk. The constant foreground reddening inside the Milky Way in the direction towards M31 is $E(B - V) = 0.08$ (Burstein & Heiles 1984) whereas the internal reddening in the disk of M31 is estimated to be $E(B - V) \approx 0.25$ (Williams & Hodge 2001) for a total reddening of $E(B - V) \approx 0.33$. Moreover, Barmby et al. (2000) find that for the M31 disk (see their Table 6), $E(B - R) \approx 1.6 \times E(B - V) \approx 0.53$. Correcting the observed $B - R$ color of M31 disk by this amount and then, using the Bell & de Jong (2001) correlations yields $M/L_R \approx 1.3$. Comparing this to the uncorrected $M/L_R \approx 3.3$ implies that the extinction in R is ~ 1.0 mag, which is in good agreement with the Kent (1989) estimate of ~ 0.99 mag for the total extinction. This agreement gives us confidence in our adopted value for the uncorrected mass-to-light of the M31 disk.

The relationship between $(M/L_R)_d$ and the disk central surface density in our models is $(M/L_R)_d = 8.46 \Sigma_{O,9}$ where $\Sigma_{O,9}$ is Σ_O in units of $10^9 M_\odot/\text{kpc}^2$. In Figure 6, we show the vertical line in the $\Sigma_0 - r_h$ plane corresponding to $M/L_R = 3.3$. We assert that suitable M31 mass models lie on the segment of this line that falls within the existing $\Delta\chi^2 = 4.0$ confidence region. In Table 2, we give the parameters for the best fit-mass model subject to the additional constraint that $(M/L_R)_d = 3.3$. We shall refer to this fit as the “ M/L -constrained” solution, and we shall use it in preference to the formal best-fit solution for the remaining discussion.

Another interesting variant is denoted by the diamond located at the intersection of the $C_{200} = 7$ and $f_{\text{gal}} = 1$ constraints. We refer to this as the “maximum disk” solution and its properties are also listed in Table 2. This solution differs from the traditional maximum disk models in that it is required to be consistent with the dynamical data *as well as* the physical constraints on the halo concentration parameter and baryonic fraction. Due to the latter two restrictions, the disk in our “maximum disk” solution does not dominate the gravitational potential to the same extent as in the traditional “maximum disk” models. The disk mass-to-light ratio of our “maximum disk” model is $M/L_R = 6.3$.

Comparing these two constrained solutions to our unconstrained results, we find that the bulge properties, such as the model mass as well as the realization of the bulge velocity dispersion and surface brightness profiles, are nearly identical. The altered surface density in the disk is offset by the halo becoming denser and more concentrated for the constrained $(M/L_R)_d = 3.3$ model, and the reverse for the maximum disk model, as seen in Figure 2 and Table 2. The overall effect is that the total rotation profiles for the constrained and the unconstrained cases are nearly the same. In the M/L -constrained model, the halo contribution to the potential is greater than that of the disk at *all* radii, a property that according to Widrow, Perrett, & Suyu (2003) and Widrow & Dubinski (2005) is likely to delay or even suppress the onset of bar formation. In contrast, the gravitational contribution of the disk in our maximum disk model is greater than that of the other two components over the radial range $5 \text{ kpc} < r < 25 \text{ kpc}$, and based on their N-body simulation studies, Widrow & Dubinski (2005) indicate that such models are highly susceptible to the formation of strong persistent bars.

4.2 Comparing to Other Mass Models

Kent (1989) was one of the first to construct a detailed mass model for M31 using both photometric and kinematic data. Comparing our M/L -constrained model (Table 2) to his small bulge model, we find that his bulge properties are in excellent agreement with ours: Kent’s bulge is a factor of ~ 1.2 more massive than ours and the corresponding mass-to-light ratio is $(M/L_R)_b = (3.7 \pm 0.4)^1$, compared to our value of 3.9. Kent’s bulge is represented as an oblate spheroid whereas our bulge is spherically symmetric, while other differences in our assumptions are detailed in § 3.1 above. In view of these differences in the models, the level of agreement in our results for the M31 bulge supports our prior assertions regarding the robustness of the bulge parameters. Kent’s disk, on the other hand, is approximately twice as massive as that of our M/L -constrained model, and the corresponding mass-to-light ratio of $(7.6 \pm 0.8)^1$ is also larger than our value of 3.3. As indicated by his Figure 2, the disk is the primary contributor to the rotation profile over the range $5 \text{ kpc} < r < 25 \text{ kpc}$ whereas in our preferred model, the disk does not dominate at any radii. However, the bulge and disk properties, including the mass-to-light ratios, of Kent’s model are similar to those of our maximum-disk model. Among the differences in our two schemes are: (a) Kent (1989) fixed the central surface brightness of his disks to values lower than what we find; and (b) he adopted a constant density dark matter halo whereas we assume an NFW functional form. The differences in our preferred results seem primarily due to assumption (b). Given these different assumptions underlying our two approaches, and the disk-halo degeneracy discussed in § 4.1, the disagreement in our disk results, at a factor ~ 2 level, is not surprising.

Widrow, Perrett, & Suyu (2003) developed their M31 model much like we did; they sought out best-fit solutions by minimizing a composite χ^2 statistic, and some of the datasets we use are taken from their paper. However, their approach differs from ours in that they modeled the disk, bulge and halo components of the galaxy as distribution functions, which cannot be specified analytically. In practise, this meant that their halo was represented by a lowered Evans model (Kuijken & Dubinski 1994; Evans 1993) instead of an NFW-like profile, their bulge by a lowered isothermal sphere or a King model (King 1966; Binney & Tremaine 1987), and their disk by a Kuijken & Dubinski (1994) model. This resembles our disk in that its surface density falls off exponentially with radius; unlike us, they also take into account the finite thickness of the disk. Widrow et al. list the properties of their best-fit model as well as a number of variants. In terms of its characteristics for $r < 30 \text{ kpc}$, our best-fit M/L -constrained model is similar to their preferred model (Model A), as can be seen by comparing their Figure 4 to our Figure 2. There are, however, some quantitative differences. Their decomposition of the surface brightness into bulge and disk components gives a bulge-to-disk light ratio of 0.58, versus our ratio of 0.38. This may stem from their different functional forms

¹ These values are slightly different from those quoted in Kent (1989) because they have been rescaled to account for the differences in our assumed distances to M31, and converted from r-band to R-band using M31 colors and $(r - R)_\odot = 0.18$ (<http://www.sdss.org/dr4/algorithms/sdssUBVRITransform.html>)

for the disk and bulge, or it may be because they use only the global surface brightness from Waltherbos & Kennicutt (1987), which does not constrain the bulge region very well. Their bulge-to-disk *mass* ratio, in contrast, is slightly smaller than ours: 0.37 versus 0.44. As a result, their bulge M/L is 2.7, 30% smaller than ours, and their disk M/L is 4.4, 33% larger than ours. The contrast between their bulge and disk M/L is not very reasonable, given that the observed disk color is slightly bluer than that of the bulge, unless there is substantial dark matter in the disk. As for the halo, Widrow et al. replace their lowered Evans model after the fact with an NFW halo that closely matches the inner structure of their original halo. This NFW halo has $C_{200} = 11.5$, $r_h = 19.5$ kpc, $R_{200} = 224$ kpc, and $M_{200} = 1.3 \times 10^{12} M_\odot$. The resulting total mass of M31 is roughly a factor of 1.8 greater than that of our system, and is somewhat on the high side in light of the mass constraints displayed in Figure 4. Nevertheless, the disk and halo properties still put their model within the allowed region in Figure 6, and in general the differences between their model and ours are not very substantial given the large differences between our functional forms.

Klypin, Zhao, & Somerville (2002) also constructed a mass and light model of M31, in order to test the consistency of large disk galaxies such as the Milky Way and M31 with the cuspy halos of the LCDM paradigm. An interesting feature of this model is the inclusion of adiabatic contraction (Blumenthal, Faber, Flores, & Primack 1986) of their *initially NFW* halos by the gravity of the disk and the bulge. To fit the baryonic component and the halo, they use a 4-component model containing a flattened bulge, a bar, an exponential disk, and the halo. This contains about 14 parameters in total. They do not actually state the parameter values or how the parameters were chosen, but they assert that these achieve a good match to the data without the need for careful optimization. Their treatment of the bulge and disk dynamics is even more approximate than ours; the central mass profile is calculated from an isothermal sphere approximation, and the disk rotation curve apparently does not take flattening into account. For this reason, some differences from our results are to be expected. Nevertheless, we find a remarkable level of agreement between their Model C1 and our best-fit constrained model, as can be seen by comparing their Figure 4 to our Figure 2. One primary difference is that their bulge-disk decomposition is different, with the mass ratio between the two only 0.27 whereas in our model it is 0.44. This could be a product of the dynamics modeling or of the different bulge profiles. A second difference is that, correcting their unextincted luminosity to extincted using the transformations they suggest, they obtain a total galaxy R luminosity of $3.5 \times 10^{10} L_\odot$ or 16% larger than ours; we do not understand the origin of this difference, since we are using nearly the same data and they have not raised the Waltherbos & Kennicutt (1987) surface brightness by 0.1 mag as we have. Together with their total baryonic component mass, which is smaller than ours by about 10%, the higher luminosity implies a total galactic (bulge+disk) mass-to-light ratio of $M/L_R = 2.5$ (extincted) whereas in our model it is 3.5. A third difference is that they use a somewhat more massive halo. Overall, we estimate that the mass of their total system within 125 kpc is approximately $0.9\text{--}1.0 \times 10^{12} M_\odot$. In our best-fit constrained model, the total mass within 125 kpc is roughly a factor of 1.5 less.

This difference is probably within the large errors on the halo mass and is not necessarily a product of our different modeling technique.

Berman (2001) and Berman & Loinard (2002) modeled the gravitational potential in the inner ~ 10 kpc of M31, using a rotating triaxial bulge. By comparing to the molecular gas flows seen in high-resolution CO velocity maps, they found a best-fit bulge mass of $2.3 \times 10^{10} M_\odot$ within 3.5 kpc (see Berman & Loinard 2002). In our three models in Table 2, the bulge mass within this radius is $2.4 \times 10^{10} M_\odot$. The agreement with the Berman & Loinard (2002) results is excellent, especially considering the complete independence of the datasets involved, and the simplifying assumptions we have made in the treatment of the bulge which (as emphasized above) is not the principal concern of our models. Berman (2001) and Berman & Loinard (2002) also estimate the disk and the total mass within 3.5 kpc to be $1.2 \times 10^{10} M_\odot$ and $3.7 \times 10^{10} M_\odot$, respectively. Given that the latter is nearly the same as the combined disk+bulge contribution, Berman & Loinard (2002) argue that the gravitational contribution of the halo within 3.5 kpc must be negligible. Our analysis, however, does not support this latter conclusion. We find that although the Berman & Loinard (2002) disk mass estimate is comparable to that in our formal best-fit and M/L-constrained models (1.1 and $1.0 \times 10^{10} M_\odot$, respectively), we require a total mass within 3.5 kpc of $5 \times 10^{10} M_\odot$, a factor of 1.35 times larger, to account for the rotation curve data. Consequently, the dark halo contributes roughly a third of the total gravity within 3.5 kpc.

In their analyses of the stream dynamics, Ibata et al. (2004) considered two variants of the Klypin, Zhao, & Somerville (2002) Model C1 in which the bulge and disk properties were kept fixed to the values specified by Klypin et al., but the halo properties were allowed to vary with the aim of minimizing discrepancies between the orbit of the progenitor and that of the giant stream. Depending on which stream constraints they used, Ibata et al. (2004) iterated to two models. The rotational velocity and the total mass profiles (computed from the rotation curve using the spherical approximation) for these two models are shown as short dashed and dot-dashed (green) lines in lower right panel of Figure 2 and in Figure 4. As illustrated in Figure 2, the rotation curve for the model dubbed “high mass” (short dashed) by Ibata et al. (2004) is in conflict with the observations. Ibata et al. (2004) note this and reject the model. The characteristics of the alternate “low mass” model (dot-dashed curve) are broadly similar to those of our constrained best-fit axisymmetric case, and for the purposes of orbit calculations, we expect that the two will give broadly similar results. However, the fact that the Ibata et al. (2004) system has 20% more mass within 125 kpc will, for a given set of initial conditions, lead to small differences in the apocenter. We discuss this point further in the next section.

Font et al. (2004), in their recent study, adopt the axisymmetric bulge-disk-halo M31 mass model of Bekki et al. (2001) with potential:

$$\Phi(r) = \Phi_b(r) + \Phi_d(r) + \Phi_h(r), \quad (16)$$

where,

$$\Phi_b(r) = -\frac{GM_b}{r_b + r}, \quad (17)$$

$$\Phi_d(r) = -\frac{GM_d}{\sqrt{R^2 + (a + \sqrt{z^2 + b^2})^2}}, \quad (18)$$

$$\Phi_h(r) = \frac{1}{2}V_h^2 \ln(r_c^2 + r^2), \quad (19)$$

r is the distance from the center of the galaxy, R and z are polar coordinates aligned with M31's disk plane, $r_c = 12$ kpc, $V_h = 186$ km s⁻¹, $M_d = 1.3 \times 10^{11}$ M_⊙, $a = 6.5$ kpc, $b = 0.26$ kpc, $M_b = 9.2 \times 10^{10}$ M_⊙, and $r_b = 0.7$ kpc. For comparative purposes, the rotation curve and the total mass profiles (computed from the rotation curve using the spherical approximation) for this model are plotted in the lower right panel of Figure 2 and in Figure 4 as long-dashed (cyan) curves. The model rotation curve is systematically higher than the observed profile, with the two being least discrepant in the outer disk region where the model curve is approximately 20 km s⁻¹ higher, and most discrepant in the inner disk. The latter is primarily due to the large bulge mass assumed by Bekki et al. (2001). Their bulge mass is a factor ~ 2.5 larger than ours. Additionally, the Bekki et al. model overestimates the the system mass beyond ~ 80 kpc. On the whole, the Bekki et al. model describes a galaxy with a much deeper potential than that indicated by the observations or that described by our preferred M31 model. As we shall illustrate in the next section, this has significant implications for orbit calculations.

To summarize, the models of the M31 potential presented in this paper seem to be more consistent with the observations than several others presented in the literature, and generally consistent with others of greater complexity while being easier to use for calculating orbits. There is, however, still a great deal of uncertainty in the actual potential. Our model, for example, is more strongly constrained in some ways by consideration of the disk mass-to-light ratio, the halo concentration, and the galaxy baryonic fraction, than by the actual observations. This uncertainty has bearing on studies of the response of the disk to perturbations, the response of dark halos to the assembly of galaxies, and the orbits of satellite galaxies, among other issues. We expect that the model can be improved in the future by the addition of more halo tracers, such as the halo stars detected by Guhathakurta et al. (2005) and Chapman et al. (in preparation); by using coherent stellar streams, such as the giant southern stream and the stream in the vicinity of NGC 205 (McConnachie et al. 2004); by the use of deep infrared surface brightness measurements, which are less sensitive to dust and stellar population variations than the optical data used here; by the incorporation of non-axisymmetric features such as the oblong/triaxial bulge and the spiral features and warping of the disk; and by properly treating the finite thickness of the disk.

5 SAMPLE ORBITS IN SPHERICAL AND FLATTENED POTENTIALS

With our mass models defined, we are now in the position to study the orbits giving rise to the giant southern stream in M31. The results of our study are described in detail in

Paper II (Fardal et al. 2005). Here, we merely present a few examples that illustrate the sensitivity of the orbits to the mass models used.

To facilitate comparison, we start by adopting initial conditions similar to those used by Font et al. (2004). These authors compute an orbit that is in rough agreement with the kinematic observations of the giant southern stream by McConnachie et al. (2003), Law, Johnston, & Majewski (2005), Ibata et al. (2004), and Guhathakurta et al. (2004). We assume here, with these authors, that the stream and the progenitor orbit are coincident. (This condition will be modified in Paper II). Font et al. define a coordinate system (x, y, z) such that the x - y plane is in the sky, with x increasing to the E and y to the N, and z is parallel to the line of sight. Font et al. locate the starting point of their orbit in the centre of the southern stream. For a detailed discussion of the stream geometry and of the choice of initial conditions, we refer the reader to Font et al. (2004) and our Paper II.

We slightly optimize the Font et al. initial conditions to better match the observations of the stream in our M/L -constrained disk potential. Specifically, we set

$$\begin{aligned} x_0 &= 14.2 \text{ kpc}, & v_{x0} &= -50 \text{ km s}^{-1}, \\ y_0 &= -33.2 \text{ kpc}, & v_{y0} &= 86.02 \text{ km s}^{-1}, \\ z_0 &= 60 \text{ kpc}, & v_{z0} &= -158 \text{ km s}^{-1}. \end{aligned}$$

For the comparisons here, the details of this optimization procedure are not important. Issues surrounding the comparison to observations will be discussed in Paper II. The primary thing to note is that the apocenter of the orbit must occur approximately at Field 1, since the z velocity of the stream relative to M31 is nearly zero there.

The main difference between the initial conditions that we use here and those used by Font et al. is that our initial velocity is not as high as theirs, because our potential for M31 is not as deep as the one they use. As a simple illustration of this point, Figure 7 shows test particle orbits calculated forward and backward from our new initial conditions, but computed in two different potentials: our M/L -constrained mass model (solid curve) and the simple singular isothermal sphere halo (dashed curve) with potential given by

$$\Phi(r) = V_c^2 \ln(r), \quad (20)$$

where $V_c = 200$ km s⁻¹ is the circular velocity. The latter is a good approximation to the model used by Font et al. in the outer halo. The key thing to note in Figure 7 is that in the deeper singular isothermal potential, the test particle is unable to climb out as far before reaching apocenter when its orbit is traced backward in time, and it falls short of Field 1 by approximately one degree. To guarantee that the apocenter of the test particle's orbit falls in Field 1 requires endowing the test particle with higher initial velocities. Since the radial velocities along the stream are observed quantities, the differences in the initial velocities will eventually result in a different assumed tilt of the orbital plane, and thus different projections of subsequent lobes of the orbit.

In Figure 8, we examine the effect of the strength of the flattened disk potential. The dotted line shows the same results for the M/L -constrained model as in Figure 7. The solid line shows the results for the *spherical disk mass model* with M/L -constrained model parameters. (We remind the reader that the halo and the bulge components of these two models are exactly the same, and even the radial mass pro-

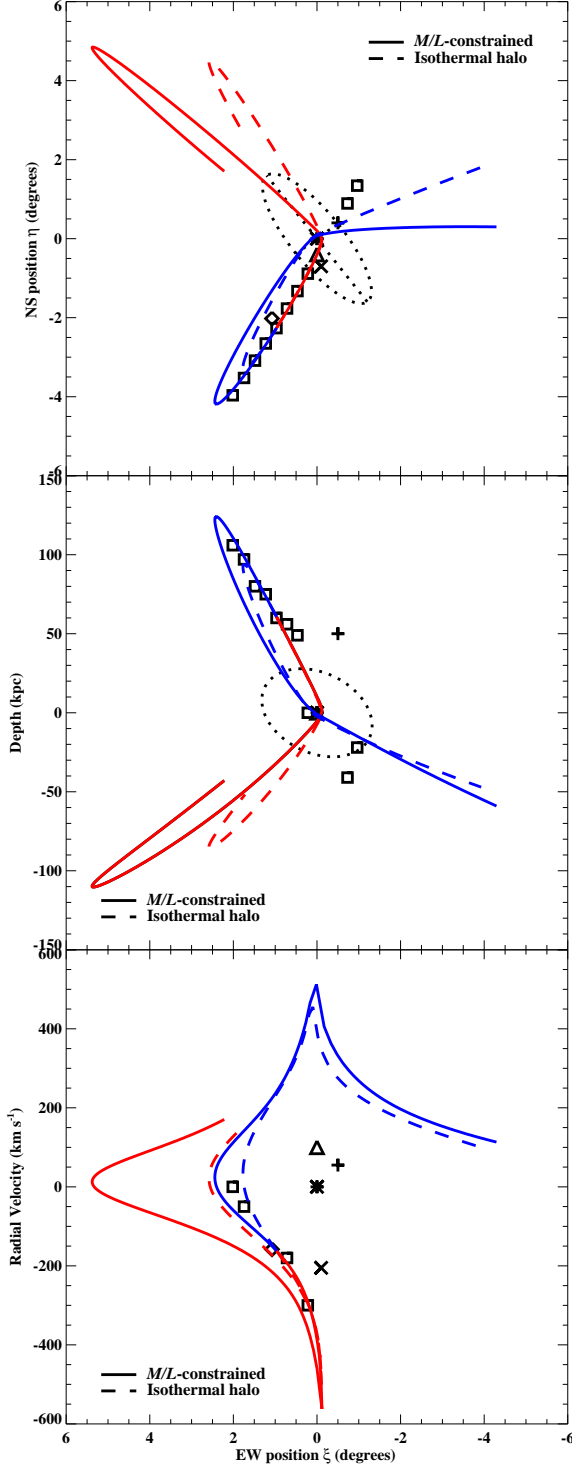


Figure 7. Comparison of test particle orbits with exactly the same initial conditions but in two different potentials: the simple singular isothermal sphere potential discussed in the text (dashed curve) and the potential corresponding to our M/L -constrained model (solid curve). The orbits are started in the centre of the southern stream with initial velocity such that the orbit in our potential turns around near Field 1. Red and blue curves represent orbit integrations forward and backward in time, respectively. (Top panel): shows the orbit in sky coordinates, ξ and η . (Middle panel): plots the line-of-sight depth (in kpc) of the orbit versus the ξ position in the sky. (Bottom panel): plots the variation of radial velocity (in km s^{-1}) with ξ position in the sky. The symbols in the three panels are as follows: star (M31), triangle (M32), plus (NGC 205), cross (And VIII), diamond (Field a3), squares (McConnachie et al. 2003 stream fields).

files of the disk component $M_d(< r)$ for the two models are the same. The only difference is that in the spherical disk case, the disk mass is distributed in a spherically symmetric fashion, as opposed to planar and axisymmetric. Consequently, the M/L -constrained spherical disk model is, as the name suggests, a spherically symmetric analog of our axisymmetric M/L -constrained model.) The result for the spherical disk model is essentially indistinguishable from the flattened disk model over the duration of the radial lobe that includes the stream. However, the directions of the preceding and subsequent lobes are different. These parts of the trajectories are very sensitive to the differences in the geometry of the disk potential at pericenter, since the test particle plunges all the way in to where the disk contribution to the total potential is significant. The gravitational pull from the disk, pulling the test particle towards the plane of the disk, results in an orbit that bends more strongly than in the spherical case. The dashed line uses the results from our “maximum disk” model. Again, the primary effect is a change in the direction of the previous and subsequent radial loops relative to the orbit in our fiducial M/L -constrained potential although in this case, the slightly deeper potential also results in a slightly smaller radial excursion at apocenter. Both of these effects are due to the stronger gravity of the disk in the maximum-disk model.

In summary, the radial mass profile has a significant effect on orbits in the halo, and is the primary factor in determining the length of the stream given the initial velocity, or alternatively the velocity gradient given the length of the stream. The geometric shape of the mass profile is a less significant factor, at least with the tests performed here, but it does significantly affect the direction of subsequent lobes. If part of the objective for computing such orbits is to try to ascertain where the progenitor might be, then ensuring that the orbits are being computed in a realistically shaped potential is important. We have neglected the possible flattening of the halo, both here and in Paper II, but this is clearly an interesting direction to explore at some point.

6 SUMMARY

The following are several significant results from this work that are important to highlight:

- We have presented a simple analytic model for the mass density, light density, and gravitational potential of M31, which is easy to use for the purposes of orbit calculations. We apply this potential in Paper II to the problem of estimating the orbit and other properties of the giant southern stream in M31’s halo.
- Our new potential does a better job matching the dynamics of M31 than other simple potentials used recently for the dynamics of the stream. It does a comparable job, and in fact is fairly similar in its properties, to several more sophisticated but non-analytic models in the literature.
- The eight parameters in our mass and light model span a large but low-dimensional region in parameter space. Physical constraints on the fraction of halo baryons in the galaxy, the halo concentration, and the stellar mass-to-light ratio restrict the parameters to a much smaller region. Our preferred model uses the M/L ratio of the disk as a further

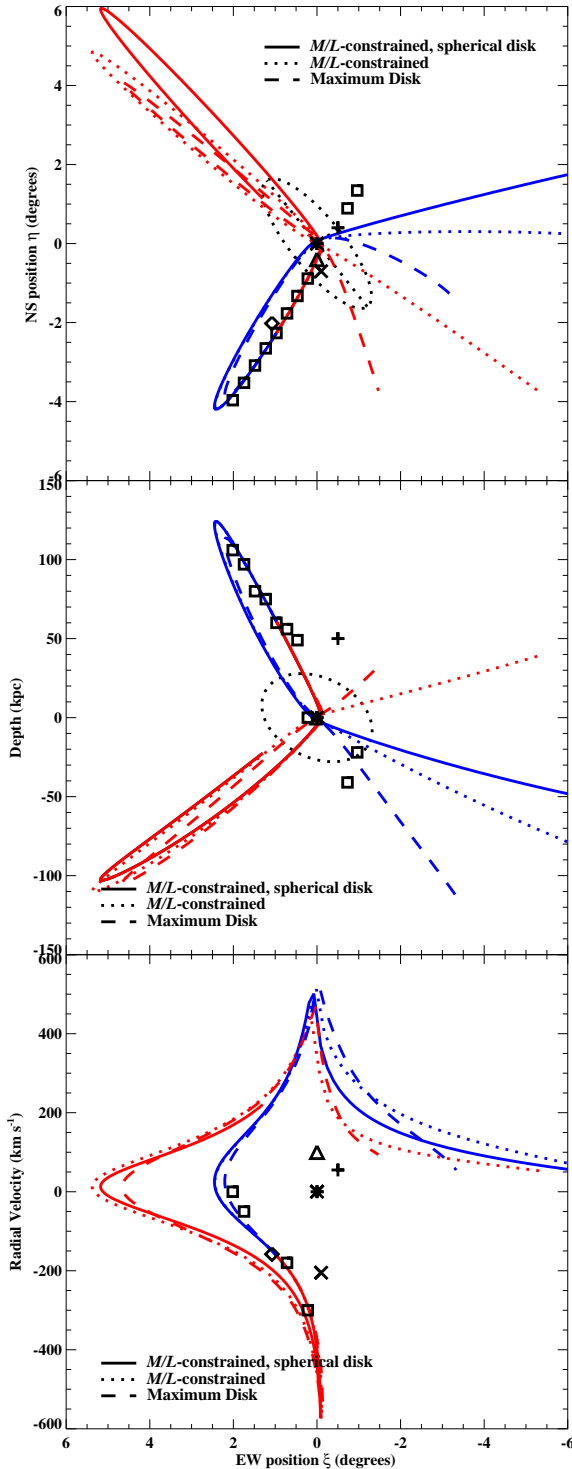


Figure 8. The above three panels show a comparison between the models with different strengths of the disk potential. All panels, symbols, and colours are the same as in Figure 7; however, the dashed line now represents the “maximum disk” model, and the solid line represents the M/L -constrained “spherical disk” model (see text for details). All orbits are calculated using the same initial conditions as in Figure 7. Note that the time intervals for the different orbits are not the same.

constraint. The parameters of this model and its important physical quantities are summarized in Table 2.

- The radial mass profile has a significant effect on orbits within the giant southern stream, and is the determining factor in the length of the stream for a given initial velocity. The geometric shape of the mass profile does not play as significant a role in determining the orbit as the radial mass profile, at least within the scope of possible variations of the disk surface density. However, it does have an effect on the direction of subsequent lobes of the orbit. This becomes important if one wishes to construct orbits for the purposes of locating the progenitor of the stream.

We are deeply grateful to Larry Widrow for kindly providing us with his data and the results of his mass model for M31. We further thank him as well as Rene Walterbos, Mark Wilkinson, Chris Pritchett, Mike Rich, Sandy Faber, Martin Weinberg, Andreea Font, Kathryn Johnston, and Laurent Loinard for helpful advice and clarifications. We are also indebted to the anonymous referee for most useful recommendations. Research support for JJG, MF and AB comes from the Natural Sciences and Engineering Research Council (Canada) through the Discovery and the Collaborative Research Opportunities grants. AB would also like to acknowledge support from the Leverhulme Trust (UK) in the form of the Leverhulme Visiting Professorship. PG is supported by NSF grant AST-0307966. He is grateful to the HIA/DAO/NRC staff for graciously hosting his 2002-03 Herzberg fellowship during which time this collaborative project was conceived.

REFERENCES

- Babcock, H. W. 1938, *PASP*, 50, 174
- Bacon, R., Emsellem, E., Combes, F., Copin, Y., Monnet, G., & Martin, P. 2001, *A&A*, 371, 409
- Barmby, P., Huchra, J. P., Brodie, J. P., Forbes, D. A., Schroder, L. L., & Grillmair, C. J. 2000, *AJ*, 119, 727
- Bekki, K., Couch, W.J., Drinkwater, M.J., & Gregg, M.D. 2001, *ApJ*, 557, L39
- Bell, E. F., & de Jong, R. S. 2001, *ApJ*, 550, 212
- Berman, S. 2001, *A&A*, 371, 476
- Berman, S., & Loinard, L. 2002, *MNRAS*, 336, 477
- Binney, J., & Tremaine, S. 1987, *Galactic Dynamics*, Princeton University Press, Princeton
- Blumenthal, G. R., Faber, S. M., Flores, R., & Primack, J. R. 1986, *ApJ*, 301, 27
- Braun, R. 1991, *ApJ*, 372, 54
- Bullock, J. S., Kolatt, T. S., Sigad, Y., Somerville, R. S., Kratsov, A. V., Klypin, A. A., Primack, J. R., & Dekel, A. 2001, *MNRAS*, 321, 559
- Burstein, D., & Heiles, C. 1984, *ApJS*, 54, 33
- Dehnaveng, J. M., & Pellet, A. 1975, *A&A*, 38, 15
- Dehnen, W. 1993, *MNRAS*, 265, 250
- Dolag, K., Bartelmann, M., Perrotta, F., Baccigalupi, C., Moscardini, L., Meneghetti, M., & Tormen, G. 2004, *A&A*, 416, 853
- Dressler, A., & Richstone, D. O. 1988, *ApJ*, 324, 701
- Dutton, A. A., Courteau, S., de Jong, R., & Carignan, C. 2005, *ApJ*, 619, 218
- Evans, N. W. 1993, *MNRAS*, 260, 191
- Evans, N. W., & Wilkinson, M. I. 2000, *MNRAS*, 316, 929

- Evans, N. W., Wilkinson, M. I., Guhathakurta, P., Grebel, E. K., & Vogt, S. S. 2000, *ApJ*, 540, L9
- Fardal, M., Babul, A., Geehan, J. J., & Guhathakurta, P. 2005, *MNRAS*, in press (Paper II)
- Ferguson, A. M. N., Irwin, M. J., Ibata, R. A., Lewis, G. F., & Tanvir, N. R. 2002, *AJ*, 124, 1452
- Ferguson, A., Chapman, S., Ibata, R., Irwin, M., Lewis, G., & McConnachie, A. 2004, in Proc. of ESO-Workshop “Planetary Nebulae beyond the Milky Way”, eds. J. R. Walsh, L. Stanghellini, Springer-Verlag (astro-ph/0408058)
- Fioc, M., & Rocca-Volmerange, B. 1997, *A&A*, 326, 950
- Font, A. S., Johnston, K. V., Guhathakurta, P., Majewski, S. R., & Rich, R. M. 2004, *AJ*, in press (astro-ph/0406146)
- Guhathakurta, P., Rich, R. M., Reitzel, D. B., Cooper, M. C., Gilbert, K., Majewski, S. R., Ostheimer, J. C., Geha, M. C., Johnston, K. V., & Patterson, R. J. 2004, *AJ*, in press (astro-ph/0406145)
- Guhathakurta et al., 2005, *Nature*, in press
- Helmi, A., & White, S. D. M. 1999, *MNRAS*, 307, 495
- Hernquist, L. 1990, *ApJ*, 356, 359
- Hoessel, J. G., & Melnick, J. 1980, *A&A*, 84, 317
- Hubble, E. 1929, *ApJ* 69, 103
- Ibata, R., Chapman, S., Ferguson, A. M. N., Irwin, M., Lewis, G., & McConnachie, A. 2004, *MNRAS*, 351, 117
- Ibata, R., Irwin, M. J., Ferguson, A. M. N., Lewis, G., & Tanvir, N. 2001, *Nature*, 412, 49
- Innanen, K. A., Kamper, K. W., van den Bergh, S., & Papp, K. A. 1982, *ApJ*, 254, 515
- Johnston, K. V., Hernquist, L., & Bolte, M. 1996, *ApJ*, 465, 278
- Jorgensen, I. 1994, *PASP*, 106, 967
- Kent, S. M. 1983, *ApJ*, 266, 562
- Kent, S. M. 1987, *AJ*, 94, 306
- Kent, S. M. 1989, *PASP*, 101, 489
- King, I. R. 1966, *AJ*, 71, 64
- Klypin, A., Zhao, H., & Somerville, R. 2002, *ApJ*, 573, 597
- Kormendy, J. 1988, *ApJ*, 325, 128
- Kormendy, J. & Bender, R. 1999, *ApJ*, 522, 772
- Kormendy, J., Richstone, D. 1995, *ARA&A*, 33, 581
- Kuijken, K. & Dubinski, J. 1994, *MNRAS*, 269, 13
- Kuzmin, G.G. 1943, *Tartu Astr. Obs. Kalender 1943*, 85 (see Einasto, J., 2004 astro-ph/0401341)
- Kuzmin, G. 1952, *Tartu Astron. Obs. Publ.*, 32, 211
- Lauer, T. R., et al. 1993, *AJ*, 106, 1436
- Law, D. R., Johnston, K. V., & Majewski, S. R. 2005, *ApJ*, 619, 807
- Lindblad, B. 1956, *Stockholm Obs. Ann.*, 19, No. 2
- Ma, J., Peng, Q., & Gu, Q. S. 1997, *ApJ*, 490, 51
- Majewski, S. R., Ostheimer, J. C., Rocha-Pinto, H. J., Patterson, R. J., Guhathakurta, P., Reitzel, D. 2004, *ApJ*, 615, 738
- Martin, N. F., Ibata, R. A., Bellazzini, M., Irwin, M. J., Lewis, G. F., Dehnen, W. 2004, *MNRAS*, 248, 12
- McConnachie, A. W., Irwin, M. J., Ibata, R. A., Ferguson, A. M. N., Lewis, G. F., & Tanvir, N. 2003, *MNRAS*, 343, 1335
- McConnachie, A. W., Irwin, M. J., Lewis, G. F., Ibata, R. A., Chapman, S. C., Ferguson, A. M. N., & Tanvir, N. R. 2004, *MNRAS*, 351, L94
- McElroy, D. B. 1983, *ApJ*, 270, 485
- Merrett, H. R., et al. 2003, *MNRAS*, 346, L62
- Merrett, H., et al. 2004, in Proc. of ESO-Workshop “Planetary Nebulae beyond the Milky Way”, eds. J. R. Walsh and L. Stanghellini, Springer-Verlag (astro-ph/0407331)
- Mo, H. J., & Mao, S. 2004, *MNRAS*, 353, 829
- Monnett, G., & Simien, F. 1977, *A&A*, 56, 173
- Morris, P. W., Reid, I. N., Griffiths, W. K., & Penny, A. J. 1994, *MNRAS*, 271, 852
- Morrison, H. L., Harding, P., Hurley-Keller, D., & Jacoby, G. 2003, *ApJ*, 596, L183
- Navarro, J. F., Frenk, C. S., & White, S. D. M. 1996, *ApJ*, 462, 563
- Newberg, H. J., et al. 2002, *ApJ*, 569, 245
- Peng, C.Y. 2002, *AJ*, 124, 294
- Press, W. H., Teukolsky, S. A., Vetterling, W. T., & Flannery, B. P. 2001, *Numerical Recipes in Fortran 77: The Art of Scientific Computing*, Cambridge University Press, New York, NY
- Pritchett, C. 1977, *ApJS*, 35, 397
- Rubin, V. C., & D’Odorico, S. 1969, *A&A*, 2, 484
- Salow, R. M., & Statler, T. S. 2004, *ApJ*, 611, 245
- Sawa, T., & Sofue, Y. 1982, *PASJ*, 34, 189
- Schmidt, M. 1957, *BAN*, 14, 17S
- Schwarzschild, M. 1954, *AJ*, 59, 273
- Simien, F., Pellet, A., & Monnet, G. 1979, *A&A*, 72, 12
- Stanek, K. Z., & Garnavich, P. M. 1998, *ApJ*, 503, 131
- Stark, A. A. 1977, *ApJ*, 213, 368
- Stark, A. A., & Binney, J. 1994, *ApJ*, 426, L31
- Tenjes, P., Haud, U., & Einasto, J. 1994, *A&A*, 286, 753
- Tremaine, S., et al. 2002, *ApJ*, 574, 740
- de Vaucouleurs, G., de Vaucouleurs, A., Corwin, H. G., Jr., Buta, R. J., & Fouque, P. 1991, *Third Reference Catalogue of Bright Galaxies*, Springer, New York
- Walterbos, R. A. M., & Kennicutt, R. C. 1987, *A&AS*, 69, 311
- Walterbos, R. A. M., & Kennicutt, R. C. 1988, *A&A*, 198, 61
- Widrow, L. M., Perrett, K. M., & Suyu, S. H. 2003, *ApJ*, 588, 311
- Widrow, L. M., Dubinski, J. 2005, *ApJ*, 631, 838
- Williams, B. F., & Hodge, P. W. 2001, *ApJ*, 548, 190
- Wyse, A. B., & Mayall, N. U. 1942, *ApJ*, 95, 24
- Wechsler, R. H., Bullock, J. S., Primack, J. R., Kravtsov, A. V., & Dekel, A. 2002, *ApJ*, 568, 52
- Weinberg, M. D., & Katz, N. 2002, *ApJ*, 580, 627
- Yanny, B., et al. 2003, *ApJ*, 588, 824
- Zucker, D. B., et al. 2004, *ApJ*, 612, L121